Inorganic Chemistry
Article
Cite This: Inorg. Chem. XXXX, XXX, XXX−XXX
pubs.acs.org/IC

$Na_2Mn_3Se_4$: Strongly Frustrated Antiferromagnetic Semiconductor with Complex Magnetic Structure

Chongin Pak,[†,#] V. Ovidiu Garlea,[*,‡] Vincent Yannello,[†] Huibo Cao,[‡] Alimamy F. Bangura,[§] and Michael Shatruk[*,†]

[†]Department of Chemistry and Biochemistry, Florida State University, Tallahassee, Florida 32306, United States
[‡]Neutron Scattering Division, Oak Ridge National Laboratory, Oak Ridge, Tennessee 37831, United States
[§]National High Magnetic Field Laboratory, 1800 East Paul Dirac Drive, Tallahassee, Florida 32310, United States

Supporting Information

ABSTRACT: A new ternary selenide, $Na_2Mn_3Se_4$, was prepared by a stoichiometric reaction between Na_2Se_4 and metallic Mn at 923 K. Crystal structure determination revealed a new structure type, built of alternating layers of Na^+ ions and $[Mn_3Se_4]^{2-}$ anionic slabs. Band structure calculations indicate that $Na_2Mn_3Se_4$ is an indirect band gap semiconductor with E_g = 1.59 eV, although a direct band gap is only marginally larger, at 1.64 eV. The material shows antiferromagnetic (AFM) ordering at 27 K, while the Weiss constant of ∼−400 K suggests much stronger nearest-neighbor AFM exchange between the Mn sites. This discrepancy is attributed to the strong spin frustration caused by a triangulated arrangement of the Mn sites in the $[Mn_3Se_4]^{2-}$ layer. The magnetic frustration leads to the stabilization of a complex AFM ordered structure with non-collinear arrangement of the Mn magnetic moments, as established from neutron diffraction data.

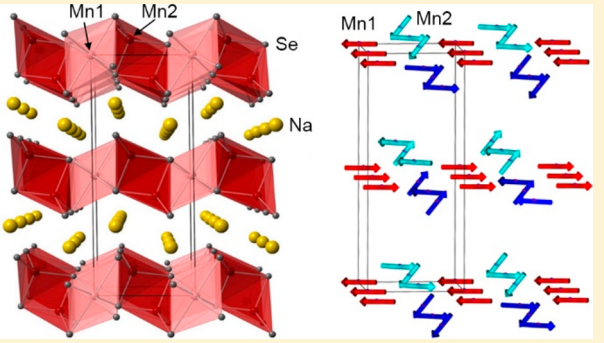

1. INTRODUCTION

Spin frustration is one of the most extensively studied topics in magnetism. A long-standing fascination with this phenomenon stems from the complexity of physics brought about by regular triangulated arrangements of interacting spins, which cannot simultaneously satisfy all magnetic exchange pathways in the case of antiferromagnetic (AFM) interactions.[1] Consequently, this phenomenon is also referred to as geometric spin frustration. In extended-structure materials, such frustrated interactions lead to highly degenerate ground states and AFM ordering temperature (T_N) that is substantially lower than could be expected from the strength of nearest-neighbor exchange interactions. The latter are characterized by the Weiss constant (θ) derived experimentally from the Curie−Weiss law. The extent of spin frustration is characterized by the frustration index, $f = |\theta|/T_N$, and systems with $f > 5-10$ are considered to be strongly frustrated. In such materials, one expects to discover ground states with complex non-collinear magnetic structures or unconventional physical behavior, e.g., such exotic states as quantum spin liquid.[2]

While spin frustration has been typically studied in systems with highly polar (ionic) bonding, which are characterized by localized and well-defined spins at each magnetic site, several works have suggested that itinerant (band) magnets or materials with more covalent bonding can also be of interest.[3] Both types of materials are characterized by magnetic moments that are substantially suppressed as compared to free-ion values. The suppression of magnetic moments, however, is compensated by delocalization of electron density from the magnetic centers onto neighboring atoms, which often promotes strong magnetic exchange. Furthermore, the next-nearest-neighbor exchange interactions also become more pronounced and can lead to frustration in the case of spins arranged on square or hexagonal lattices.[3d,4]

Transition metal selenides and tellurides represent a borderline behavior between the metallic and insulating systems. They exhibit sufficient electronegativity difference in the metal−chalcogen bonds to form electronic structures with finite band gaps (semiconductors), yet the covalency of bonding is also substantial, which results in partially suppressed magnetic moments but stronger magnetic exchange coupling. This trend can be visualized, for example, by contrasting the increasing AFM ordering temperatures for MnO (118 K), MnS (140 K), MnSe (247 K), and MnTe (307 K)[5] with the decreasing magnetic moment per Mn atom (5.65 μ_B,[6] 4.39 μ_B,[7] 3.30 μ_B,[8] and 2.06 μ_B,[9] respectively) in the AFM ordered state of these compounds.[10]

The interest in magnetically frustrated systems with appreciable covalent bonding has led us to examine alkali-metal manganese selenides, the crystal structures of which contain triangular arrangements of Mn sites and thus are

Received: January 14, 2019

DOI: 10.1021/acs.inorgchem.9b00134
Inorg. Chem. XXXX, XXX, XXX−XXX

conducive to magnetic frustration in the case of AFM exchange. Indeed, Kim and Hughbanks reported highly negative (AFM) Weiss constants for a number of such compounds.[11] In particular, $NaMnSe_2$ and $Na_2Mn_2Se_3$ were characterized by θ values of −1000 and −140 K, respectively, but the first showed AFM ordering only at 9 K while for the second no magnetic ordering was observed down to 4 K. Intrigued by this brief report, we set out to examine more thoroughly the magnetic behavior of $Na_2Mn_2Se_3$, which seems to exhibit very strong magnetic frustration ($f > 35$). In the course of these studies, we discovered a new ternary compound, $Na_2Mn_3Se_4$, and established that it exhibits a layered structure with strong magnetic exchange between Mn sites and AFM ordering at 27 K. The pronounced magnetic frustration in this material is also caused by a triangulated arrangement of Mn magnetic moments, which leads to the formation of a complex magnetic structure below T_N, as shown in this work.

2. MATERIALS AND METHODS

Synthesis. Sodium pieces (99.95%), manganese powder (99.95%, 325 mesh), and selenium powder (99.999%, 200 mesh) were obtained from Alfa Aesar and used as received. All sample preparation procedures were carried out in an argon-filled glovebox (content of O_2 < 1 ppm). To prepare Na_2Se_4, stoichiometric amounts of sodium and selenium were sealed under vacuum (<10^{-5} Torr) in a 10 mm inner diameter (i.d.)/12 mm outer diameter (o.d.) fused silica tube. The sealed tube was first carefully heated with a hand-held torch to premix the reactants, and then it was placed into a furnace, heated to 923 K at a rate of 10 K/min, maintained at that temperature for 2 days, and quenched into water bath. The phase purity of the Na_2Se_4 precursor was confirmed by powder X-ray diffraction (PXRD). The starting materials in the stoichiometric Na_2Se_4:Mn = 1:3 molar ratio, with the total mass of 0.3−0.5 g, were thoroughly mixed by grinding in an agate mortar and loaded into a 12.7 mm o.d. graphite crucible, which was sealed under vacuum (<10^{-5} Torr) in a 16 mm i.d./14 mm o.d. fused silica tube. The mixture was heated to 923 at 0.2 K/min, maintained at that temperature for 4 days, and cooled to room temperature at 2 K/h.

Caution! *(1) Prior to use, sodium pieces were carefully scraped with a scalpel to remove the surface layer of oxide. After the shavings were taken out of the drybox, they were immediately covered with methanol to avoid a violent reaction of any traces of Na with moist air. (2) The synthesis of Na_2Se_4 was performed under slow heating, to allow sufficient time for dissipation of heat generated by the exothermic reaction between Na and Se.*

X-ray Diffraction. Room temperature PXRD was performed on a Panalytical X'pert Pro diffractometer equipped with an X'Celerator detector and a CuK_α radiation source (λ = 1.54187 Å). The HighScore Plus[12] and FullProf[13] software packages were used for profile fitting and unit cell refinement.

Single crystal X-ray diffraction (SCXRD) was performed on a Bruker APEX-II CCD X-ray diffractometer equipped with a graphite-monochromated MoK_α radiation source (λ = 0.71073 Å). A single crystal was suspended in Paratone-N oil (Hampton Research) inside a cryoloop which was mounted on a goniometer head and cooled to 173 K in a cold stream of N_2 gas. The data set was recorded as ω- and φ-scans at 0.3° step width and integrated with the Bruker SAINT software package.[14] A multi-scan empirical adsorption correction was applied based on multiple equivalent measurements (SADABS).[15] The space group determination was performed with XPREP,[16] and the crystal structure solution and refinement were carried in the $C2/m$ space group, using the SHELX program suite.[17] The final refinement was performed with anisotropic atomic displacement parameters for all atoms. A summary of pertinent information relating to unit cell parameters, data collection, and refinement is provided in Table 1.

Table 1. Crystallographic Data for $Na_2Mn_3Se_4$

compound		$Na_2Mn_3Se_4$
ICSD code		433906
temp, K		173
λ, Å		0.71073
space group		$C2/m$
unit cell	a, Å	15.8555(3)
	b, Å	4.0734(1)
	c, Å	6.4327(1)
β, deg		90.810(1)
V, Å^3		415.42(1)
Z		2
crystal color		dark-red
crystal size, mm^3		0.11 × 0.068 × 0.064
d_{calcd}, g cm^{-3}		4.210
μ, mm^{-1}		22.017
θ_{max}, deg		47.59
reflections collected		3019
R_{int}		0.0175
unique reflections		983
parameters refined		30
R_1, $wR_2[F > 4\sigma(F)]$[a]		0.019, 0.045
goodness-of-fit[b]		1.132
diff. peak and hole, e Å^{-3}		1.11, −1.28

[a] $R_1 = \sum||F_o| - |F_c||/\sum|F_o|$; $wR_2 = [\sum[w(F_o^2 - F_c^2)^2]/\sum[w(F_o^2)^2]]^{1/2}$. [b] Goodness-of-fit $= [\sum[w(F_o^2 - F_c^2)^2]/(N_{obs} - N_{params})]^{1/2}$, based on all data.

Neutron Diffraction. Powder and single-crystal neutron diffraction experiments were performed at the High Flux Isotope Reactor at Oak Ridge National Laboratory (ORNL). Powder diffraction measurements were carried out using the HB-2A high-resolution diffractometer.[18] Data were collected on a sample of ∼3 g held in a cylindrical vanadium container placed in a top-loading closed cycle refrigerator, covering a temperature range of 1.7−150 K. The λ = 1.539 Å monochromatic radiation was provided by a vertically focused Ge (115) monochromator. The data were collected by scanning the detector array consisting of 44 ^{3}He tubes, to cover the total 2θ range of 7°−133° in steps of 0.05°. Overlapping detectors for a given step served to average the counting efficiency of each detector.

Single-crystal neutron diffraction was performed on the HB-3A four-circle diffractometer.[19] Neutrons with wavelength of λ = 1.005 Å were selected by a bent silicon monochromator Si-331. The data were collected at 4 and 100 K. Intensities of selected magnetic peaks were also measured as a function of temperature to determine the magnetic ordering temperature. Refinement of the nuclear structure and magnetic structure determination were carried out using the FULLPROF software.[13]

Physical Measurement. Elemental analysis of selected single crystals was performed on a FEI Nova NanoSEM 400 scanning electron microscope with Oxford INCA energy dispersive X-ray (EDX) analysis system. Optical absorption was measured on a single crystal under Parabar oil (Hampton Research) with FLEX micro-spectrophotometer (Craic Technologies). Magnetic property measurements were carried out on oriented single crystals and microcrystalline powder samples with Quantum Design SQUID magnetometer MPMS XL7. The temperature dependence of magnetization was measured in the 1.8−400 K temperature range under applied direct-current (DC) magnetic field of 0.5 T. The field-dependent magnetization was measured at 1.8 K with the applied DC field varying from 0 to 7 T.

Quantum-Chemical Calculations. Density-functional theory (DFT) calculations were performed using a full-potential all-electron local orbital code (version FPLO-14)[20] within the generalized gradient approximation (GGA) with GGA+U approach. The Perdew−Wang parametrization of the exchange-correlation potentials

DOI: 10.1021/acs.inorgchem.9b00134
Inorg. Chem. XXXX, XXX, XXX−XXX

was employed.[21] The solution of scalar-relativistic Dirac equation was obtained self-consistently. The tetrahedron method was used for the Brillouin zone integration.[22] The structural parameters (unit cell dimension and atomic coordinates) were taken from the experimentally determined crystal structure data. The spin-polarized densities of state (DOS) were calculated after convergence of the total energy on a dense *k*-mesh with 16×16×16 points. The self-consistent criterion for the total energy conversion was set to 10^{-8} Ha ($\sim 2.72 \times 10^{-7}$ eV). The optimal values of *U* (3.0 eV) and *J* (1.0 eV) were obtained empirically by varying both parameters to match the measured band gap as closely as possible while still having realistic Mn−Se band mixing. To simplify the calculations, the Mn magnetic moments were chosen to be AFM aligned along the [011] direction.

3. RESULTS AND DISCUSSION

Synthesis. Phase-pure $Na_2Mn_3Se_4$ was obtained in both polycrystalline powder and single crystal form. The stoichiometric reaction between the binary precursor, Na_2Se_4, and metallic Mn was found to be a more efficient way for the preparation of a single-phase product, as compared to the direct reaction between constituent elements, which led to the presence of MnSe and $Na_2Mn_2Se_3$ impurities. Slow cooling (at 2 K/h) of the reaction mixture from 923 K to room temperature afforded rod-shaped crystals of ∼2×1×1 mm^3 size. The obtained product is air- and moisture-sensitive, hence the sample has to be handled under inert (Ar) atmosphere. The phase purity was confirmed by PXRD (Figure 1). The composition of single-crystalline samples was confirmed by EDX elemental analysis, which resulted in the Na:Mn:Se ratio of 2.0(1):3.1(2):3.9(1).

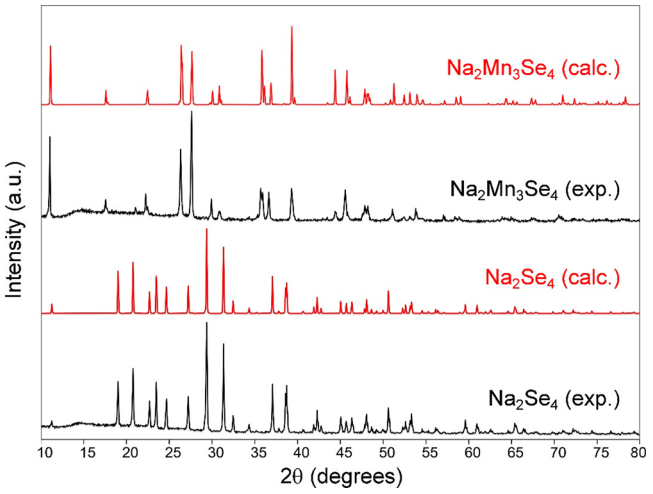

Figure 1. Experimental (black) and calculated (red) powder X-ray diffraction patterns of $Na_2Mn_3Se_4$ and Na_2Se_4. (The low-angle background is caused by scattering from an airtight sample holder.)

Crystal Structure. $Na_2Mn_3Se_4$ crystallizes in the monoclinic space group *C*2/*m* (Table 1) and represents a new structure type. The structure can be viewed as an arrangement of alternating $[Mn_3Se_4]^{2-}$ layers and Na^+ ions (Figure 2a). Since no Se−Se bonds are observed in the structure, the charge-balance considerations indicate the presence of only Mn^{2+} ions. The $[Mn_3Se_4]^{2-}$ layers are built of octahedra and tetrahedra of Se atoms centered around Mn1 and Mn2 sites, respectively (Figure 2b and Table 2). The $MnSe_6$ octahedra share edges to form chains along the *b* axis, while the $MnSe_4$ tetrahedra form edge-sharing dimers which share corners to form chains along the *b* axis. These parallel chains of octahedra

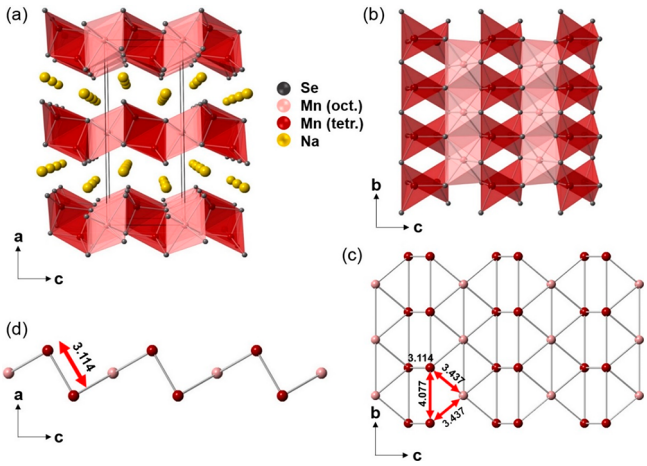

Figure 2. (a) A view of the crystal structure of $Na_2Mn_3Se_4$, showing anionic $[Mn_3Se_4]^{2-}$ layers alternating with layers of Na^+ cations. (b) The $[Mn_3Se_4]^{2-}$ layer is formed by chains of $MnSe_6$ octahedra connected via dimers of $MnSe_4$ tetrahedra. The Mn sites in one layer are arranged into strips of triangles (c) that form a zigzag slab when viewed down the *b* axis (d). The Mn−Mn distances (in Å) within one triangle and between the adjacent strips are indicated.

Table 2. Atomic Sites of $Na_2Mn_3Se_4$

site	Wyckoff position	*x*	*y*	*z*	$U_{iso} \times 10^2$
Na1	4*i*	0.29803(7)	0.5	0.2340(2)	1.91(3)
Mn1	2*a*	0	0	0	1.66(1)
Mn2	4*i*	0.08434(2)	0.5	0.37921(6)	0.855(8)
Se1	4*i*	−0.06489(2)	0.5	0.22820(3)	0.726(7)
Se2	4*i*	0.16002(2)	0	0.24530(4)	0.999(7)

and tetrahedra are connected to each other by edge sharing to form layers parallel to the *bc* plane. Each octahedron shares two and four edges with neighboring octahedra and tetrahedra, respectively. The $MnSe_4$ tetrahedron is slightly distorted, with Mn2−Se bonds ranging from 2.5218(3) to 2.5485(4) Å. In contrast, the $MnSe_6$ octahedron exhibits a substantial axial elongation, with the equatorial and axial Mn1−Se bonds at 2.7211(2) and 2.9689(2) Å, respectively. The distorted octahedral coordination of the Mn1 site is also reflected in its atomic displacement ellipsoid, which is elongated along the axial direction (Figure S1). While such elongation might appear counterintuitive for the electronically isotropic high-spin Mn^{2+} ion, it is not unusual in such extended structures due to crystal packing effects. Our analysis of the Inorganic Crystal Structure Database for the structures containing $MnSe_6$ octahedra revealed non-negligible distortions in ∼40% of cases. For examples, large distortions are observed in the structures of $UMnSe_3$ and U_8MnSe_{17}.[23]

The Mn sites (Table 2) within each $[Mn_3Se_4]^{2-}$ layer can be viewed as forming stripes of edge-sharing triangles, with the octahedral Mn sites occurring in the center of the stripe and the tetrahedral Mn1 sites being at its periphery (Figure 2c). The stripes, which run along the *b* axis, are connected to each other in a step-like fashion (Figure 2d), forming the layers that are parallel to the *bc* plane. The shortest Mn−Mn distances occur within the dimers of edge-sharing tetrahedra (3.112 Å) and between the tetrahedral and octahedral Mn centers (3.434 Å), while the Mn−Mn distances within the chain of edge-sharing octahedra are longer (4.073 Å). The shorter Mn−Mn separations, however, form a continuous 2D network, which

DOI: 10.1021/acs.inorgchem.9b00134
Inorg. Chem. XXXX, XXX, XXX−XXX

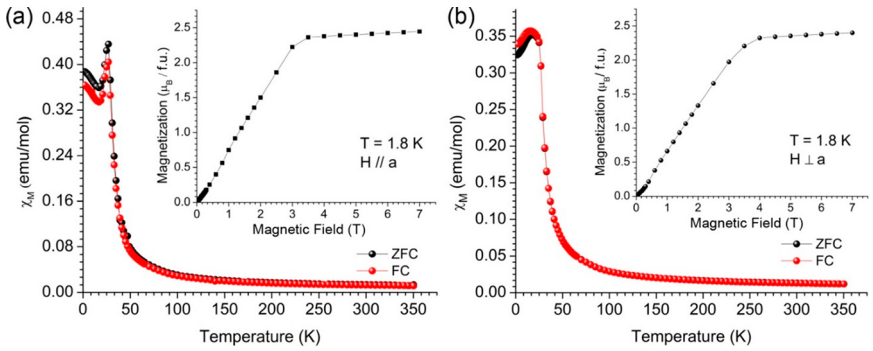

Figure 3. Temperature-dependent FC (red curves) and ZFC (black curves) magnetic susceptibility and field-dependent magnetization (insets) measured on a single crystal of $Na_2Mn_3Se_4$ with the magnetic field applied parallel (a) or perpendicular (b) to the *a* axis.

might be important to understanding the magnetic behavior of $Na_2Mn_3Se_4$.

As has been already mentioned, $Na_2Mn_3Se_4$ represents a new ternary structure type. While several other $A_2T_3X_4$ chalcogenides are known (A = K, Rb, Cs, T = 3d metal, X = S, Se, Te), the majority of them crystallize in the orthorhombic (*Ibam*) $Cs_2Zn_3S_4$ structure type.[24] In particular, this structure is common to the $A_2Mn_3X_4$ compounds (A = K, Rb, Cs),[25] although $K_2Mn_3S_4$ crystallizes in its own structure type,[26] representing a stacking variant of the $Cs_2Zn_3S_4$ type. In these structures, $[Mn_3X_4]^{2-}$ layers also alternate with layers of A^+ cations (Figure S2a), but the transition metal layers are flat and contain only tetrahedrally coordinated Mn^{II} sites, with each MnX_4 tetrahedron sharing edges with three or two neighbor tetrahedra (Figure S2b). Interestingly, the $Na_2Mn_3Se_4$ structure is the first example of the $A_2T_3X_4$ phase with A = Li or Na. Moreover, such stoichiometry is more common for A = Rb or Cs as compared to A = K. This observation suggests that the $Cs_2Zn_3S_4$-type structure, probably, becomes unstable for the smaller alkali metal ions, which could explain the more complicated structure of the $[Mn_3Se_4]^{2-}$ layers in $Na_2Mn_3Se_4$: the corrugation of the layers might be necessary to accommodate coordination preferences of the smaller Na^+ ions (Figure 2a).

Magnetic Properties. The crystal structure described above reveals the presence of extensively triangulated arrangement of Mn sites, which can cause strong magnetic frustration in the Mn sublattice in the case of antiferromagnetic (AFM) nearest-neighbor interactions. Magnetic properties were studied on a 1.5×0.5×0.5 mm^3 single crystal of $Na_2Mn_3Se_4$, with the magnetic field (H) of 0.5 T applied either parallel or perpendicular to the *a* axis, which means, respectively, perpendicular or parallel to the $[Mn_3Se_4]^{2-}$ layers. For both field orientations, the ZFC and FC magnetic susceptibility curves diverged at the maximum value, suggesting AFM ordering at about 27 K (Figure 3). For the field applied parallel to the *a* axis, the susceptibility exhibits a sharp decrease and is followed by a rise. This could correspond to a subtle spin reorientation that involves the change of the moment projection along the *a* axis.

The FC susceptibility and its inverse were fit to the Curie–Weiss law (Figure S3), $\chi = C/(T - \theta) + \chi_0$, where C is the Curie constant, θ is the Weiss constant, and χ_0 is temperature-independent paramagnetism. The fit turned out to be very sensitive to χ_0, due to the relatively limited linear range available in the high-temperature region. Therefore, the value of χ_0 was averaged from several fitting attempts and fixed at 0.001 emu·K/mol. The effective magnetic moment, obtained from the partially constrained Curie–Weiss fit, was calculated as $\mu = (8C)^{1/2}$, resulting in the values of $\mu_{\parallel} = 5.73(3)\ \mu_B$ ($H \| a$) and $\mu_{\perp} = 5.56(3)\ \mu_B$ ($H \perp a$) per Mn^{2+} ion, Both of these values are slightly lower than the value of 5.92 μ_B expected for the high-spin (S = 5/2) Mn^{2+} ion. The Weiss constant was equal to −402(15) K for $H \| a$ and −352(6) K for $H \perp a$, thus indicating strong AFM interactions between Mn sites. The spin-frustration index, $f = |\theta|/T_N$, averages to ∼28, which corresponds to strong magnetic frustration.[2]

Isothermal field-dependent magnetization of $Na_2Mn_3Se_4$ was measured at 1.8 K. A very similar behavior was observed for both crystal orientations (Figure 3, insets), suggesting negligible magnetic anisotropy in the system. For both orientations of the applied field, the magnetization reaches a plateau of ∼2.4 μ_B per formula unit (f.u.) at around 4 T. This magnetization value (∼0.8 μ_B per Mn^{2+} ion) is substantially smaller than the maximum of 5 μ_B that can be achieved for a single high-spin Mn^{2+} ion. We also carried out magnetization measurements at higher field to probe the stability of the magnetization plateau. Increasing the field to 16 T did not produce any substantial changes in the slope of the magnetization dependence (Figure S4). The remarkable stability of this plateau region with the rather low total magnetization value suggests that the AFM ordered state might exhibit an unconventional magnetic structure due to the strongly frustrated AFM interactions between Mn magnetic moments.

We used neutron diffraction to establish the magnetic structure of $Na_2Mn_3Se_4$. Powder neutron diffraction measurements revealed the emergence of a long-range magnetic order defined by two distinct propagation vectors, $\boldsymbol{k}_1$ = (1/2,1/2,1/2) and $\boldsymbol{k}_2$ = (1,0,0). Figure 4a shows the pure magnetic contribution to the low-angle scattering observed at 1.7 K, which was obtained by subtracting the nuclear contribution measured in the paramagnetic state at 60 K. The existence of two sets of magnetic reflections corresponding to the double-$\boldsymbol{k}$ magnetic structure has also been confirmed by single crystal diffraction measurements on a 2.0×1.0×1.0 mm^3 crystal of $Na_2Mn_3Se_4$. The magnetic order parameter was obtained by measuring the change in the intensity of the (3,0,0) and (3/2,1/2,−1/2) magnetic reflections upon cooling across the AFM transition temperature (Figure 4b). At T_N, the magnetic peak associated with $\boldsymbol{k}_1$ exhibits a more rapid increase in intensity as compared to the $\boldsymbol{k}_2$-related peak. Furthermore, after reaching the saturation, the (3/2,1/2,−1/2) peak displays a dip at around 17 K, which is consistent with the spin

DOI: 10.1021/acs.inorgchem.9b00134
Inorg. Chem. XXXX, XXX, XXX−XXX

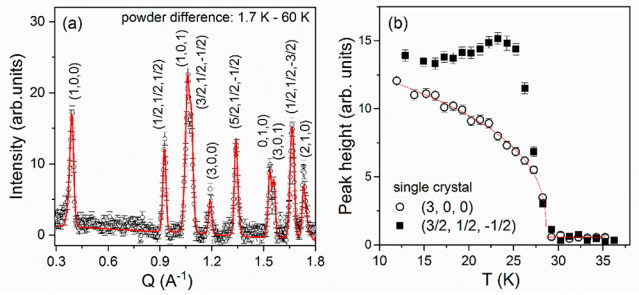

Figure 4. (a) Magnetic scattering at 1.7 K obtained by subtracting the nuclear contribution measured at 60 K. The red lines represent the Rietveld fit using the magnetic structure model described in the text. The magnetic peaks were indexed with two propagation vectors, $\boldsymbol{k}_1$ = (1/2,1/2,1/2) and $\boldsymbol{k}_2$ = (1,0,0). (b) Temperature-dependent intensity of magnetic Bragg peaks (3,0,0) (open circles) and (3/2,1/2,−1/2) (solid squares) obtained from single crystal measurements. The solid red line is a guide to the eye.

reorientation suggested by magnetization data. The discrepancy in the temperature evolution for the two sets of reflections suggests distinct arrangements of magnetic moments in the two nonequivalent Mn sites. The lower sensitivity of the (3,0,0) reflection to the upturn of magnetization below 17 K might indicate that the spin reorientation occurs within the *bc* plane.

Magnetic structure models that can result from a second-order magnetic phase transition have been explored by representation analysis using the program SARAh.[27] There are two possible irreducible representations (IRs) associated with the *C*2/*m* space group and $\boldsymbol{k}_1$ = (1/2,1/2,1/2). The magnetic representation for the octahedrally coordinated Mn1 site (0,0,0) is decomposed as $\Gamma_{Mag} = 3\Gamma_1$ while for the tetrahedral Mn2 site (*x*,0,*z*) it is $\Gamma_{Mag} = 3\Gamma_1 + 3\Gamma_2$. For the propagation vector $\boldsymbol{k}_2$ = (1,0,0) there are four possible IRs, which give $\Gamma_{Mag} = \Gamma_1 + 2\Gamma_3$ for the Mn1 site and $\Gamma_{Mag} = \Gamma_1 + 2\Gamma_2 + 2\Gamma_3 + \Gamma_4$ for the Mn2 site. Table 3 summarizes these IRs and the basis vectors associated with each of the two observed ***k***-vectors.

The magnetic peak intensities measured at 1.7 K are best described by a model where the moments located at the octahedral Mn1 sites order according to the $\boldsymbol{k}_2$ propagation vector, while the moments on the tetrahedral Mn2 sites order with a double-***k*** structure described by both $\boldsymbol{k}_1$ and $\boldsymbol{k}_2$ propagation vectors. The Mn1 moments are confined to the *bc* plane (Figure 2a) and their description involves mixing the basis vectors of Γ_1 and Γ_3 (see the Ψ_i associated with $\boldsymbol{k}_2$ = (100) in Table 3). The magnetic order breaks the *C*-centering present in the atomic structure, and magnetic moments of the atoms related by the (1/2,1/2,0) translation become aligned antiparallel to each other. Overall, the magnetic sublattice composed of Mn1 atoms exhibits AFM stacking of ferromagnetic layers along the *a* axis (Figure 5a, red arrows).

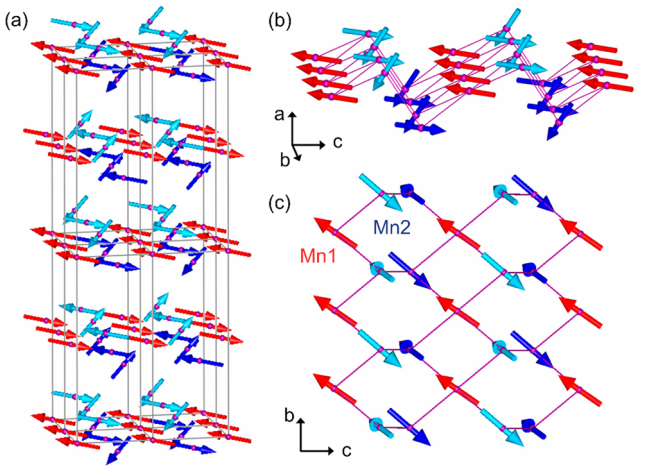

Figure 5. (a) Magnetic structure of $Na_2Mn_3Se_4$ at 1.7 K. The Mn1 magnetic sublattice (red arrows) exhibits AFM stacking of ferromagnetically ordered planes along the *a* axis. The Mn2 magnetic sublattice (blue and light-blue arrows) doubles along all three crystallographic axes and exhibits noncollinear arrangement of magnetic moments. (b) Stereoscopic view of magnetic ordering in a single $[Mn_3Se_4]^{2-}$ layer. (c) Projection of the magnetic structure of the $[Mn_3Se_4]^{2-}$ layer on the *bc* plane.

The refined projections of the Mn1 magnetic moments on the unit cell axes are m_a = 0.3(2) μ_B, m_b = 2.2(2) μ_B, and m_c= 3.2(1) μ_B, resulting in the total magnetic moment of 3.9(2) μ_B.

In contrast to the Mn1 site, the magnetic moment distribution on the Mn2 sites is more complicated, given the

Table 3. Irreducible Representations (IRs) and Basis Vectors (Ψ_i) Associated with the Space Group *C*2/*m* and the Two Propagation Vectors $\boldsymbol{k}_1$ = (1/2,1/2,1/2) and $\boldsymbol{k}_2$ = (1,0,0) Observed for $Na_2Mn_3Se_4$[a]

			Mn1 (2*a*) (0,0,0)			Mn2 (4*i*) (*x*,0,*z*)		
k-vector	IR	atom number	Ψ_1	Ψ_2	Ψ_3	Ψ_1	Ψ_2	Ψ_3
(1/2,1/2,1/2)	Γ_1	1	(1,0,0)	(0,1,0)	(0,0,1)	(1,0,0)	(0,1,0)	(0,0,1)
		2				(1,0,0)	(0,1,0)	(0,0,1)
	Γ_2	1				(1,0,0)	(0,1,0)	(0,0,1)
		2				(−1,0,0)	(0,−1,0)	(0,0,−1)
(1,0,0)	Γ_1	1		(0,1,0)			(0,1,0)	
		2					(0,1,0)	
	Γ_2	1				(1,0,0)		(0,0,1)
		2				(−1,0,0)		(0,0,−1)
	Γ_3	1	(1,0,0)		(0,0,1)	(1,0,0)		(0,0,1)
		2				(1,0,0)		(0,0,1)
	Γ_4	1					(0,1,0)	
		2					(0,−1,0)	

[a]The equivalent Mn2 atoms of the non-primitive basis are defined according to 1:(0.415, 0, 0.621) and 2:(0.584, 0, 0.379).

DOI: 10.1021/acs.inorgchem.9b00134
Inorg. Chem. XXXX, XXX, XXX−XXX

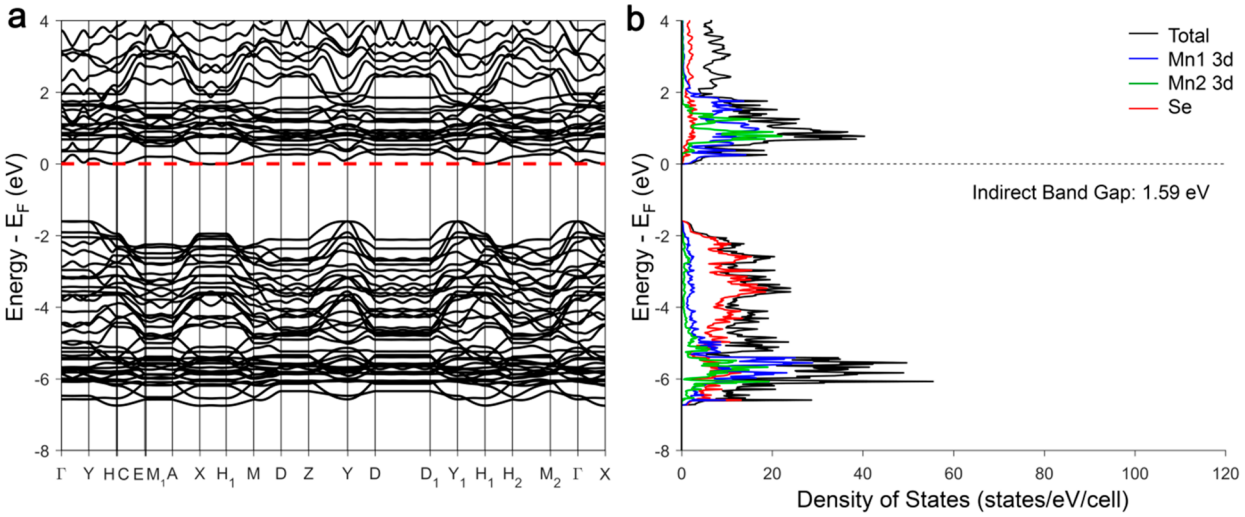

Figure 6. Electronic band structure (a) and spin-polarized density of states (b) for $Na_2Mn_3Se_4$. In each plot, the Fermi level is indicated with a dashed line.

concomitant presence of two propagation vectors. The Mn2 magnetic sublattice doubles along all three crystallographic directions and loses the mirror symmetry, which leads to splitting of the crystallographic Mn2 (4*i*) site in two distinct magnetic positions with non-collinear arrangement of magnetic moments. As depicted in Figure 5, the moment direction alternates along the *b* axis, between a nearly antiparallel orientation relative to the neighboring Mn1 moments and an out-of-plane orientation with respect to the *bc* plane. The refined in-plane and out-of-plane magnetic moments (and their projections) are equal to 4.1(1) μ_B (m_a = 0.2, m_b = 2.7, m_c = 3.1 μ_B) and 3.3(2) μ_B (m_a = 2.5, m_b = 1.2 m_c = 1.7 μ_B), respectively, indicating that the out-of-plane Mn2 moments are canted at 41° relative to the *a* axis. The reduced amplitude of the static moments at one of the corners of the triangulated Mn lattice is likely a consequence of the strong geometric frustration. The moments distribution within each $[Mn_3Se_4]^{2-}$ layer is shown in Figure 5b,c. Overall, the Mn1 and Mn2 moments form ferrimagnetic layers that are stacked AFM along the *a* axis, in agreement with the AFM ordering observed in the magnetic measurements.

As mentioned above, the field-dependent magnetization measured at 2 K (Figure S1) revealed the gradual increase in magnetization followed by the plateau at 2.4 μ_B per f.u. The remarkable stability of this plateau region is in agreement with the strong AFM coupling between the Mn moments, while the nature of the initial linear increase in magnetization is not yet clear. A possible explanation could be gradual rotation of the out-of-plane Mn2 moments to attain a nearly collinear arrangement with the Mn1 and Mn2 moments arranged parallel to the *bc* plane. On the other hand, the single-crystal magnetic measurements suggest that the entire magnetic structure corresponding to the plateau region might be following the magnetic field direction, since no much difference is observed between the magnetization measured parallel and perpendicular to the *a* axis. The magnetic structure achieved in the plateau region will have to be elucidated by neutron diffraction measurements under applied magnetic field.

We can also envision an alternative explanation for the observed magnetic behavior of $Na_2Mn_3Se_4$. An examination of interatomic distances shows the substantially shorter separation (3.114 Å) between the tetrahedral Mn2 sites of the neighboring triangulated strips (Figure 2c) as compared to the Mn1−Mn2 (3.437 Å) or Mn1−Mn1 and Mn2−Mn2 (4.077 Å) distances within the same strip (Figure 2d). Thus, it is possible that the large negative Weiss constant is primarily caused by the strong AFM coupling within the interstrip dimers, while the weaker AFM coupling operates along the longer intrastrip Mn−Mn exchange pathways, causing the substantially lower ordering temperature. Such situation, nevertheless, can still be considered as frustration (also not the ideal geometric one), due to the competing exchange interactions that manifest themselves in the formation of the complex spin texture in the magnetically ordered state of $Na_2Mn_3Se_4$.

Electronic Structure. The electronic band structure calculations revealed the band gap of 0.60 eV, which was substantially smaller than the value of ∼2.0 eV established from the onset of optical absorption measured on a single crystal of $Na_2Mn_3Se_4$ (Figure S5). The under-estimation of the band gap is a common problem of DFT methods.[28] To mitigate this issue, the empirical Hubbard parameter (U) was included in calculations and varied to approach the experimentally determined band gap. We observed, however, that higher values of U led to nearly complete separation in energy between the Mn and Se states (Figure S6), which is rather unrealistic, given the substantial degree of covalent bonding between these elements. Therefore, a compromise was reached between matching the experimental E_g value and maintaining mixing between the Mn and Se states. The optimal value of U = 3 eV resulted in E_g = 1.59 eV (Figure 6a). Additionally, the experimentally determined magnetic structure exhibits a complex noncollinear ordering of the Mn magnetic moments, whereas in the electronic structure calculations we used a simpler collinear AFM arrangement of the Mn moments along the [011] direction, which might also affect the calculated band gap. The DOS curve reveals nearly complete polarization of the Mn1 and Mn2 3*d* states below the Fermi energy (Figure 6b). The occupied Mn 3*d* states show significant interactions with the Se valence orbitals, while the lower region of the conduction band is comprised predominantly of Mn 3*d* states, with higher lying states (>2 eV above E_F) having significant Se and Na contributions.

DOI: 10.1021/acs.inorgchem.9b00134
Inorg. Chem. XXXX, XXX, XXX−XXX

Due to the monoclinic symmetry of the structure, many special points appear in the first Brillouin zone, which immensely complicates the band structure. Additionally, the lowest unoccupied band and the highest occupied band nearly reach their minimum/maximum at many of these points. While the band gap is found to be indirect and equal to 1.59 eV, the direct band gap at the Γ point is only slightly larger, at 1.64 eV. Lowering the *U* parameter below 3 eV maintains the location of the indirect band gap, while increasing *U* above 3 eV switches the band structure to a direct bandgap at Γ. This finding suggests that the nature of the band gap in this material might be sensitive to small perturbations of its crystal structure. Our future studies will focus on doping various sublattices of $Na_2Mn_3Se_4$ to probe the stability of its magnetic structure and the possible switching to the direct band gap semiconductor, which might promote photoluminescent properties.

4. CONCLUSIONS

In summary, a new layered-structure selenide, $Na_2Mn_3Se_4$, exhibits triangulated arrangement of the Mn sites, which are engaged in strong AFM exchange interactions, as evidenced by the large and negative value of the Weiss constant (∼ − 400 K). As a result, the material displays strong magnetic frustration, manifested in the much lower AFM ordering temperature of 27 K. As mentioned in the Introduction, large negative Weiss constants of −1000 K and −140 K were also reported for $NaMnSe_2$ and $Na_2Mn_2Se_3$, respectively.[1] Given that the former showed AFM ordering only at 9 K and the latter did not exhibit magnetic ordering down to 4 K, we find the magnetic frustration indices $f = 111$ for $NaMnSe_2$ and $f > 35$ for $Na_2Mn_2Se_3$. These values warrant further detailed investigation of these and related materials. Such studies are currently under way in our laboratories.

Neutron diffraction studies revealed a complex magnetic structure of $Na_2Mn_3Se_4$. The arrangement of ordered magnetic moments in the Mn sites is described by two propagation vectors, which result in both in-plane and out-of-plane arrangement of moments with respect to the orientation of the $[Mn_3Se_4]^{2-}$ layers. Overall, the Mn moments form ferrimagnetic layers which are stacked AFM along the *a* axis. Interestingly, applied magnetic field appears to stabilize another non-collinear arrangement of Mn moments, as suggested by a low-moment magnetization plateau observed between 4 and 16 T. Thus, it is of interest to study the magnetic structure of this material in the plateau region, which we plan to do by means of powder neutron diffraction under applied magnetic field. The results of these studies will be reported in due course.

■ ASSOCIATED CONTENT

Supporting Information

The Supporting Information is available free of charge on the ACS Publications website at DOI: 10.1021/acs.inorgchem.9b00134.

Anisotropic displacement ellipsoids for $Na_2Mn_3Se_4$, crystal structure of $Rb_2Mn_3Se_4$, additional magnetic plots, optical absorption spectrum, and band structure and density of states diagrams for $Na_2Mn_3Se_4$, including Figures S1−S6 (PDF)

Accession Codes

CCDC 1891813 contains the supplementary crystallographic data for this paper. These data can be obtained free of charge via www.ccdc.cam.ac.uk/data_request/cif, or by emailing data_request@ccdc.cam.ac.uk, or by contacting The Cambridge Crystallographic Data Centre, 12 Union Road, Cambridge CB2 1EZ, UK; fax: +44 1223 336033.

■ AUTHOR INFORMATION

Corresponding Author

*E-mail: shatruk@chem.fsu.edu.

ORCID

Michael Shatruk: 0000-0002-2883-4694

Present Address

#C.P.: Applied Superconductivity Center, National High Magnetic Field Laboratory, 1800 E. Paul Dirac Dr., Tallahassee, FL 32310-3706, USA

Notes

The authors declare no competing financial interest.

■ ACKNOWLEDGMENTS

This work was supported by the National Science Foundation via award DMR-1507233 to M.S. The work at the ORNL was sponsored by the Scientific User Facilities Division, Office of Basic Energy Sciences, U.S. Department of Energy. We thank Dr. Shane Galley for assistance with optical spectroscopy.

■ REFERENCES

(1) Ramirez, A. P. Strongly geometrically frustrated magnets. *Annu. Rev. Mater. Sci.* **1994**, *24*, 453−480.

(2) Balents, L. Spin liquids in frustrated magnets. *Nature* **2010**, *464*, 199−208.

(3) (a) Ballou, R.; Lelièvre-Berna, E.; Fåk, B. Spin fluctuations in $(Y_{0.97}Sc_{0.03})Mn_2$: a geometrically frustrated, nearly antiferromagnetic, itinerant electron system. *Phys. Rev. Lett.* **1996**, *76*, 2125−2128. (b) Koyama, T.; Yamashita, H.; Takahashi, Y.; Kohara, T.; Watanabe, I.; Tabata, Y.; Nakamura, H. Frustration-induced valence bond crystal and its melting in Mo_3Sb_7. *Phys. Rev. Lett.* **2008**, *101*, 12640. (c) Nakatsuji, S.; Machida, Y.; Maeno, Y.; Tayama, T.; Sakakibara, T.; Van Duijn, J.; Balicas, L.; Millican, J. N.; Macaluso, R. T.; Chan, J. Y. Metallic spin-liquid behavior of the geometrically frustrated kondo lattice $Pr_2Ir_2O_7$. *Phys. Rev. Lett.* **2006**, *96*, 087204. (d) Sapkota, A.; Ueland, B. G.; Anand, V. K.; Sangeetha, N. S.; Abernathy, D. L.; Stone, M. B.; Niedziela, J. L.; Johnston, D. C.; Kreyssig, A.; Goldman, A. I.; McQueeney, R. J. Effective one-dimensional coupling in the highly frustrated square-lattice itinerant magnet $CaCo_{2-y}As_2$. *Phys. Rev. Lett.* **2017**, *119*, 147201.

(4) Nguyen, S.; Ryan, K.; Chai, P.; Shatruk, M.; Xin, Y.; Chapman, K. W.; Chupas, P. J.; Fronczek, F. R.; Macaluso, R. T. $Pr_{1.33}Pt_4Ga_{10}$: Superstructure and magnetism. *J. Solid State Chem.* **2014**, *220*, 9−16.

(5) Squire, C. F. Antiferromagnetism in some manganous compounds. *Phys. Rev.* **1939**, *56*, 922−925.

(6) Goodwin, A. L.; Tucker, M. G.; Dove, M. T.; Keen, D. A. Magnetic structure of MnO at 10 K from total neutron scattering data. *Phys. Rev. Lett.* **2006**, *96*, 047209.

(7) Masrour, R.; Hlil, E. K.; Hamedoun, M.; Benyoussef, A.; Mounkachi, O. Study of electronic and magnetic properties of MnS layers. *Chin. Phys. B* **2012**, *21*, 127101.

(8) Ingle, K. E.; Efrem D'Sa, J. B. C.; Das, A.; Priolkar, K. R. Structural and magnetic phase transitions in MnTe-MnSe solid solutions. *J. Magn. Magn. Mater.* **2013**, *347*, 68−71.

(9) Efrem D'Sa, J. B. C.; Bhobe, P. A.; Priolkar, K. R.; Das, A.; Paranjpe, S. K.; Prabhu, R. B.; Sarode, P. R. Low-temperature neutron diffraction study of MnTe. *J. Magn. Magn. Mater.* **2005**, *285*, 267−271.

(10) We should point out that there is still a debate about the true value of the magnetic moment per Mn site in MnSe and MnTe. The problem is related, in part, to different polymorphs and structural

DOI: 10.1021/acs.inorgchem.9b00134
Inorg. Chem. XXXX, XXX, XXX−XXX

phase transitions shown by these materials. See, for example, ref 9 as well as the following: Szuszkiewicz, W.; Hennion, B.; Witkowska, B.; Łusakowska, E.; Mycielski, A. Neutron scattering study of structural and magnetic properties of hexagonal MnTe. *Phys. Status Solidi C* **2005**, *2*, 1141−1146.
(11) Kim, J.; Hughbanks, T. Synthesis and structures of new layered ternary manganese selenides: $AMnSe_2$ (A = Li, Na, K, Rb, Cs) and $Na_2Mn_2Se_3$. *J. Solid State Chem.* **1999**, *146*, 217−225.
(12) *X-Pert HighScore Plus software v. 2.2b*; PANalytical B.V.: Almelo, The Netherlands, 2006.
(13) Rodríguez-Carvajal, J. Recent advances in magnetic-structure determination by neutron powder diffraction. *Phys. B* **1993**, *192*, 55−69.
(14) *SMART and SAINT*; Bruker AXS Inc.: Madison, WI, USA, 2007.
(15) Sheldrick, G. M. *SADABS*; University of Gottingen: Gottingen, Germany, 1996.
(16) Sheldrick, G. M. *XPREP. Space group determination and reciprocal space plots*; Siemens Analytical X-ray Instruments: Madison, WI, USA, 1991.
(17) Sheldrick, G. M. A short history of SHELX. *Acta Crystallogr., Sect. A: Found. Crystallogr.* **2008**, *A64*, 112−122.
(18) Garlea, V. O.; Chakoumakos, B. C.; Moore, S. A.; Taylor, G. B.; Chae, T.; Maples, R. G.; Riedel, R. A.; Lynn, G. W.; Selby, D. L. The high-resolution powder diffractometer at the High Flux Isotope Reactor. *Appl. Phys. A: Mater. Sci. Process.* **2010**, *99*, 531−535.
(19) Chakoumakos, B. C.; Cao, H.; Ye, F.; Stoica, A. D.; Popovici, M.; Sundaram, M.; Zhou, W.; Hicks, J. S.; Lynn, G. W.; Riedel, R. A. Four-circle single-crystal neutron diffractometer at the High Flux Isotope Reactor. *J. Appl. Crystallogr.* **2011**, *44*, 655−658.
(20) Koepernik, K.; Eschrig, H. Full-potential nonorthogonal local-orbital minimum-basis band-structure scheme. *Phys. Rev. B: Condens. Matter Mater. Phys.* **1999**, *59*, 1743.
(21) Perdew, J. P.; Wang, Y. Accurate and simple analytic representation of the electron-gas correlation-energy. *Phys. Rev. B: Condens. Matter Mater. Phys.* **1992**, *45*, 13244.
(22) Blochl, P. E.; Jepsen, O.; Andersen, O. K. Improved tetrahedron method for Brillouin-zone integrations. *Phys. Rev. B: Condens. Matter Mater. Phys.* **1994**, *49*, 16223.
(23) Noel, H. Selenium compounds of uranium in the systems USe_2-MSe (M = Mg, Ti, V, Cr, Mn, Fe, Co, Ni). *C. R. Ser. C* **1974**, *279*, 513−15.
(24) Bronger, W.; Hendriks, U. Preparation and crystal structure of $Cs_2Zn_3S_4$ and $Rb_2Zn_3S_4$. *Rev. Chim. Miner.* **1980**, *17*, 555−560.
(25) (a) Bronger, W.; Böttcher, P. Thiomanganates and thiocobaltates of heavy alkaline metals - $Rb_2Mn_3S_4$, $Cs_2Mn_3S_4$, $Rb_2Co_3S_4$, $Cs_2Co_3S_4$. *Z. Anorg. Allg. Chem.* **1972**, *390*, 1−12. (b) Bronger, W.; Hardtdegen, H.; Kanert, M.; Müller, P.; Schmitz, D. Alkali metal manganese selenides and tellurides - synthesis, crystal and spin structures. *Z. Anorg. Allg. Chem.* **1996**, *622*, 313−318.
(26) Bronger, W.; Böhmer, M.; Schmitz, D. Synthesis and crystal structure of $K_2Mn_3S_4$. *Z. Anorg. Allg. Chem.* **2000**, *626*, 6−8.
(27) (a) Wills, A. S. A new protocol for the determination of magnetic structures using simulated annealing and representational analysis (SARAh). *Phys. B* **2000**, *276−278*, 680−681. (b) Perez-Mato, J. M.; Gallego, S. V.; Tasci, E. S.; Elcoro, L.; de la Flor, G.; Aroyo, M. I. Symmetry-based computational tools for magnetic crystallography. *Annu. Rev. Mater. Res.* **2015**, *45*, 217−248.
(28) Perdew, J. P.; Levy, M. Physical content of the exact Kohn-Sham orbital energies: band gaps and derivative discontinuities. *Phys. Rev. Lett.* **1983**, *51*, 1884−1887.

DOI: 10.1021/acs.inorgchem.9b00134
Inorg. Chem. XXXX, XXX, XXX−XXX